Editors' Suggestion

Magnetic microstructure of nanocrystalline Fe-Nb-B alloys as seen by small-angle neutron and x-ray scattering

Venus Rai [1,*] Ivan Titov [1] Michael P. Adams [1] Kiyonori Suzuki [2] Joachim Kohlbrecher [3] and Andreas Michels [1,†]

[1] *Department of Physics and Materials Science, University of Luxembourg, 162A avenue de la Faiencerie, L-1511 Luxembourg, Grand Duchy of Luxembourg*

[2] *Department of Materials Science and Engineering, Monash University, Clayton, VIC 3800, Australia*

[3] *Paul Scherrer Institute, CH-5232 Villigen PSI, Switzerland*

(Received 24 May 2024; accepted 7 August 2024; published 23 August 2024)

We have investigated the magnetic microstructure of two-phase Fe-Nb-B based Nanoperm alloys using unpolarized small-angle neutron scattering (SANS) and small-angle x-ray scattering (SAXS). Our SANS analysis reveals a significantly large magnetic scattering contribution due to spin misalignment, primarily originating from the substantial jump in the longitudinal magnetization at the interfaces between the particles and the matrix. The magnetic scattering exhibits an angular anisotropy that resembles a clover-leaf-type pattern, consistent with the predictions of micromagnetic SANS theory. Analysis of the one-dimensional SANS data yields values for the exchange-stiffness constant and the average anisotropy and magnetostatic fields. The micromagnetic correlation lengths for all three samples exhibit a similar field variation with sizes ranging between about 10–35 nm. We also find that the nuclear and magnetic residual scattering component of the SANS cross section exhibits a similar q dependency as the SAXS data. These findings further validate the applicability of the micromagnetic SANS theory, and the mesoscopic information obtained is important for the advancement of the soft magnetic properties of this class of material.

DOI: 10.1103/PhysRevB.110.054437

I. INTRODUCTION

Iron-based soft ferromagnetic alloys with an ultrafine-grained microstructure attract a lot of attention because of their high saturation magnetization, low coercivity, and low core losses (see, e.g., Refs. [1–12] and references therein). These properties result in their great potential for various technological applications, such as in turbine generators, high-frequency power transformers, interface transformers, or various consumer electronics devices. However, in order to build energy-efficient devices, core losses have to be minimized, which can be achieved by minimizing the magnetic anisotropy and increasing the saturation magnetization.

Recent studies of soft magnetic Fe-B based Nanoperm alloys have shown that, in addition to magnetic hysteresis and eddy current losses, significant core (power) losses in Nanoperm may arise due to magnetostriction as well [13,14]. This excess loss is attributed to factors such as domain walls, inelastic lattice relaxation mediated by magnetostriction, and magnetic interactions, including spin misalignment due to longitudinal magnetization jumps. Understanding and enhancing functionality requires scrutinizing the grain and magnetic microstructures on a mesoscopic length scale, where many macroscopic magnetic properties are realized.

Small-angle neutron scattering (SANS) emerges as a key experimental technique, offering insights into the magnetic microstructure within a range of ∼1–1000 nm [15,16]. Due to the high penetrating power of neutrons, thick bulk samples can commonly be investigated. Moreover, the past two decades have witnessed a significant progress regarding the understanding of magnetic SANS, which enables the quantitative study of the mesocale magnetic microstructure of a wide range of nanocrystalline compounds (e.g., [17–35]).

Here, we report SANS and small-angle x-ray scattering (SAXS) results on a series of Fe-based nanocrystalline alloys ($Fe_{87}B_{13}$, $Fe_{85}Nb_6B_9$, $Fe_{80}Nb_6B_{14}$). We observe a significant variation of the SANS cross section as the applied magnetic field is reduced from 9 T down to about 0.1 T, which demonstrates the presence of a large spin-misalignment scattering in all the samples. The two-dimensional magnetic SANS signal exhibits an anisotropic clover-leaf-type pattern, in agreement with the prevalence of dipolar stray fields decorating the nanoparticles, in this way producing nanoscale spin disorder.

The paper is organized as follows: Section II furnishes some details on the neutron experiment as well as on the structural and magnetic properties of the Nanoperm alloys. Section III sketches the basic ideas of the micromagnetic SANS theory, as it is implemented in the *MuMag2022* software tool [36] used for the neutron data analysis. Section IV features the neutron data and analysis, the ensuing results for the exchange constants and the average anisotropy and magnetostatic fields, and a comparison of the residual SANS cross section with laboratory SAXS data. Finally, in

*Contact author: venus.rai@uni.lu

†Contact author: andreas.michels@uni.lu

TABLE I. Structural and magnetic properties of the investigated Nanoperm alloys. Data partially taken from Ref. [14].

Alloy	Annealing condition	Annealing temperature	Thickness	Grain size	H_c (A/m)	$\mu_0 M_0$ (T)	λ_s (ppm)
$Fe_{87}B_{13}$	Ultra-rapid annealing	753 K (0.5 sec.)	13.8 µm	16 nm	7.3	1.89	13
$Fe_{85}Nb_6B_9$	Tube annealing	898 K (30 min.)	14.5 µm	11 nm	6.7	1.67	∼0
$Fe_{80}Nb_6B_{14}$	Tube annealing	898 K (30 min.)	24.5 µm	10 nm	3.9	1.50	2.4

Sec. V we summarize the main findings of this study. The Appendix displays the complete set of the two-dimensional total (nuclear and magnetic) and purely magnetic SANS cross sections of the Nanoperm alloys.

II. EXPERIMENTAL

Nanoperm samples with nominal compositions of $Fe_{87}B_{13}$, $Fe_{85}Nb_6B_9$, and $Fe_{80}Nb_6B_{14}$ were prepared by rapid solidification (melt spinning) followed by thermal annealing. This resulted in ultrafine-grained microstructures consisting of nanocrystalline Fe particles that are embedded in an amorphous Nb-B magnetic matrix. For the sample synthesis, the low neutron absorbing isotope ^{11}B was used. The details of the sample preparation can be found in Refs. [14,37]. Further information on the annealing conditions during the synthesis procedure of each sample as well as the structural and magnetic properties are given in Table I.

The unpolarized SANS experiment was performed using the SANS-I instrument at the Swiss Spallation Neutron Source at the Paul Scherrer Institute, Switzerland. A schematic drawing of the SANS experiment is depicted in Fig. 1. We used an incident mean neutron wavelength of $\lambda = 6$ Å with a wavelength broadening of $\Delta\lambda/\lambda = 10\,\%$ (FWHM). For the SANS experiment, typically 10–15 sheets of Nanoperm were stacked together, resulting in total sample thicknesses of ∼150–250 µm (compare to Table I). The entire SANS experiment was conducted at room temperature and under the application of an external magnetic field ($\mu_0 H_0^{\max} = 9$ T), applied along the horizontal direction and perpendicular to the incoming neutron beam (compare to Fig. 1). The SANS intensity for each sample was recorded at three different sample-to-detector distances (2 m, 6 m, 18 m), enabling data collection in a q range of ∼0.03–3 nm^{-1}. The neutron data reduction (corrections for background scattering and sample transmission) was conducted using the GRASP software package [38].

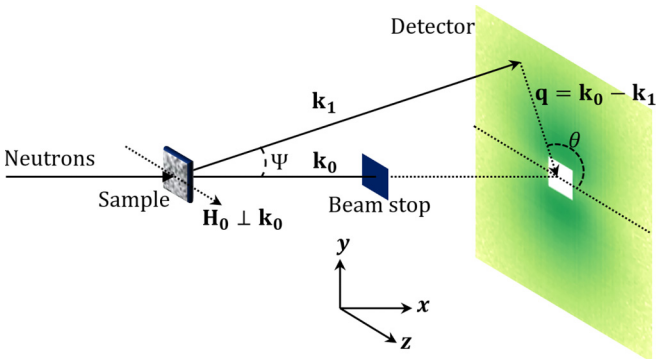

FIG. 1. Schematic drawing of the SANS setup. The wave vectors of the incoming and scattered neutron beams are, respectively, denoted by $\mathbf{k}_0$ and $\mathbf{k}_1$, and ψ denotes the scattering angle. The momentum-transfer or scattering vector equals $\mathbf{q} = \mathbf{k}_0 - \mathbf{k}_1$. The azimuthal angle θ describes the angular anisotropy of the scattered neutron intensity on the 2D detector. The direction of the applied magnetic field $\mathbf{H}_0$ is horizontal and perpendicular to the incident beam. In our notation, $\mathbf{H}_0$ defines the z axis of a Cartesian global frame, the incoming beam ($\mathbf{k}_0$) is along the x axis, and the vertical direction defines the y axis.

Wide-angle x-ray diffraction measurements of all the samples were performed in a Bruker D8 DISCOVER diffractometer setup in Bragg-Brentano geometry using Cu-K_α radiation ($\lambda = 0.154$ nm). Characteristic Bragg peaks corresponding to the pure Fe phase (BCC) were observed. The full-width at half maxima (FWHM) of these peaks was analyzed, and the average crystallite size was estimated using the Scherrer equation. The obtained particle sizes (grain sizes) are given in Table I. Furthermore, all three samples were characterized by small-angle x-ray scattering (SAXS) using an Anton Paar SAXSpoint 5.0 instrument. Monochromatic x-rays with a wavelength of $\lambda = 0.154$ nm were used to investigate the Nanoperm samples at scattering vectors $q = 4\pi \sin(\psi/2)/\lambda$ ranging from about 0.045 nm^{-1} to 2.1 nm^{-1}, where ψ denotes the scattering angle (compare to Fig. 1).

Room temperature magnetization measurements were performed using a Cryogenics Ltd. vibrating sample magnetometer setup, equipped with a 14 T superconducting magnet. The normalized magnetization data are displayed in Fig. 2. As mentioned in Table I, the saturation magnetizations of all three samples are significantly different [14]. However, the approach-to-saturation regime [$M/M(14\,\mathrm{T}) \gtrsim 95\,\%$] is, for all three samples, attained for applied fields larger than about 0.1 T. This should guarantee the validity of the micromagnetic SANS analysis. Magnetic parameters are listed in Table I.

III. MAGNETIC SANS THEORY

The total unpolarized SANS cross section of a bulk ferromagnet consists of nuclear and magnetic scattering contributions. The origin of magnetic SANS are mesoscale spatial variations in the magnitude and orientation of the magnetization vector field $\mathbf{M}(\mathbf{r}) = \{M_x(\mathbf{r}), M_y(\mathbf{r}), M_z(\mathbf{r})\}$, where M_z denotes the longitudinal magnetization (parallel to $\mathbf{H}_0$), and $M_{x,y}$ are the two transversal components [15,16]. The Nanoperm alloys studied in this paper are magnetically extremely soft, implying that a very small field of the order of a

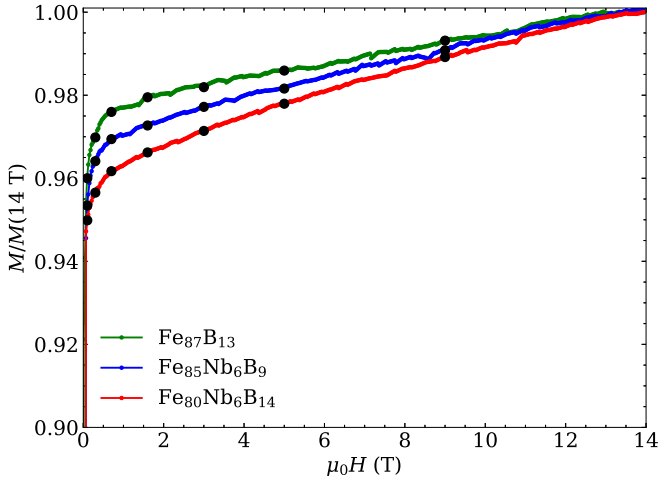

FIG. 2. Normalized room-temperature magnetization curves of the Nanoperm samples (see inset; only the upper right quadrant is shown). The black dots mark the field values of the SANS measurements.

few mT will bring the material close to magnetic saturation. In this case the magnetic small-angle scattering due to the M_z fluctuations can be approximated to be independent of the applied magnetic field, while the magnetic SANS due to the $M_{x,y}$, called spin-misalignment scattering, is strongly field dependent, in particular at small momentum transfers. The micromagnetic SANS theory that is here used to analyze the Nanoperm alloys is detailed in Refs. [39,40] and implemented in the *MuMag2022* software tool [36]. In the following, we recall the basic expressions to achieve a self-contained presentation.

As shown in Ref. [39], near magnetic saturation, the total unpolarized SANS cross section $d\Sigma/d\Omega$ can be evaluated by means of micromagnetic theory. In particular,

$$\frac{d\Sigma}{d\Omega}(\mathbf{q}) = \frac{d\Sigma_{\text{res}}}{d\Omega}(\mathbf{q}) + \frac{d\Sigma_{\text{M}}}{d\Omega}(\mathbf{q}), \tag{1}$$

where

$$\frac{d\Sigma_{\text{res}}}{d\Omega}(\mathbf{q}) = \frac{8\pi^3}{V}\left(|\widetilde{N}|^2 + b_{\text{H}}^2|\widetilde{M}_z|^2\sin^2\theta\right), \tag{2}$$

represents the nuclear and magnetic residual SANS cross section, which is measured at complete magnetic saturation (infinite field), and

$$\frac{d\Sigma_{\text{M}}}{d\Omega}(\mathbf{q}) = S_{\text{H}}(\mathbf{q})\,R_{\text{H}}(q,\theta,H_{\text{i}}) + S_{\text{M}}(\mathbf{q})\,R_{\text{M}}(q,\theta,H_{\text{i}}) \tag{3}$$

is the spin-misalignment SANS cross section. In Eq. (2), V is the scattering volume, $b_{\text{H}} = 2.91\times10^8\,\text{A}^{-1}\text{m}^{-1}$ is the magnetic scattering length, $\widetilde{N}(\mathbf{q})$ and $\widetilde{\mathbf{M}}(\mathbf{q}) = \{\widetilde{M}_x(\mathbf{q}), \widetilde{M}_y(\mathbf{q}), \widetilde{M}_z(\mathbf{q})\}$ denote, respectively, the Fourier transforms of the nuclear scattering-length density and of the magnetization $\mathbf{M}(\mathbf{r})$, and θ represents the angle between $\mathbf{H}_0$ and $\mathbf{q}$ (see Fig. 1). The magnetic scattering due to transversal spin components, with related Fourier amplitudes $\widetilde{M}_x(\mathbf{q})$ and $\widetilde{M}_y(\mathbf{q})$, is contained in $d\Sigma_{\text{M}}/d\Omega$, which decomposes into a contribution $S_{\text{H}}R_{\text{H}}$ due to perturbing magnetic anisotropy fields and a part $S_{\text{M}}R_{\text{M}}$ related to magnetostatic fields. The micromagnetic SANS theory considers a uniform exchange interaction and a random distribution of the magnetic easy axes, as it is appropriate for a statistically isotropic polycrystalline ferromagnet [16]. Spatial variations in the magnitude of the saturation magnetization are explicitly taken into account via the function S_{M} (see below). Moreover, in the approach-to-saturation regime it is assumed that $|\widetilde{M}_z|^2 = |\widetilde{M}_{\text{s}}|^2$, where $\widetilde{M}_{\text{s}}(\mathbf{q})$ denotes the Fourier transform of the saturation magnetization profile $M_{\text{s}}(\mathbf{r})$.

Regarding the decomposition of the SANS cross section [Eq. (1)], it is important to emphasize that it is $d\Sigma_{\text{M}}/d\Omega$ which depends on the magnetic interactions (exchange, anisotropy, magnetostatics), while $d\Sigma_{\text{res}}/d\Omega$ is determined by the geometry of the underlying grain microstructure (e.g., the particle shape or the particle-size distribution). If in a SANS experiment the approach-to-saturation regime can be reached for a particular magnetic material (as it is the case for the Nanoperm alloys), then the residual SANS can be obtained by an analysis of field-dependent data via the extrapolation to infinite field. In a sense, for a bulk ferromagnet, the scattering at saturation resembles the topographical background in Kerr-microscopy experiments, which needs to be subtracted in order to access the magnetic domain structure of the sample [41].

The anisotropy-field scattering function (in units of cm^{-1})

$$S_{\text{H}}(\mathbf{q}) = \frac{8\pi^3}{V}\,b_{\text{H}}^2\,|\widetilde{\mathbf{H}}_{\text{p}}|^2 \tag{4}$$

depends on $\widetilde{\mathbf{H}}_{\text{p}}(\mathbf{q})$, which represents the Fourier transform of the spatial structure of the magnetic anisotropy field $\mathbf{H}_{\text{p}}(\mathbf{r})$ of the sample, whereas the scattering function of the longitudinal magnetization (in units of cm^{-1})

$$S_{\text{M}}(\mathbf{q}) = \frac{8\pi^3}{V}\,b_{\text{H}}^2\,|\widetilde{M}_z|^2 \tag{5}$$

provides information on the spatial variation of the saturation magnetization $M_{\text{s}}(\mathbf{r})$; for instance, in a multiphase magnetic nanocomposite, $S_{\text{M}} \propto |\widetilde{M}_z|^2 \propto (\Delta M)^2$, where ΔM denotes the jump of the magnetization magnitude at internal (particle-matrix) interfaces. Note that the volume average of $M_{\text{s}}(\mathbf{r})$ equals the macroscopic saturation magnetization $M_0 = \langle M_{\text{s}}(\mathbf{r})\rangle$ of the sample, which can be measured with a magnetometer. The corresponding dimensionless micromagnetic response functions can be expressed as [39]

$$R_{\text{H}}(q,\theta,H_{\text{i}}) = \frac{p^2}{2}\left(1 + \frac{\cos^2\theta}{(1+p\sin^2\theta)^2}\right) \tag{6}$$

and

$$R_{\text{M}}(q,\theta,H_{\text{i}}) = \frac{p^2\,\sin^2\theta\cos^4\theta}{(1+p\sin^2\theta)^2} + \frac{2p\,\sin^2\theta\cos^2\theta}{1+p\sin^2\theta}, \tag{7}$$

where

$$p(q,H_{\text{i}}) = \frac{M_0}{H_{\text{eff}}(q,H_{\text{i}})} \tag{8}$$

is a dimensionless function, and θ represents the angle between $\mathbf{H}_0 = H_0\mathbf{e}_z$ and $\mathbf{q} \cong q\{0, \sin\theta, \cos\theta\}$. The effective magnetic field

$$H_{\text{eff}}(q, H_\text{i}) = H_\text{i}\left(1 + l_\text{H}^2 q^2\right) = H_\text{i} + \frac{2A}{\mu_0 M_0} q^2 \tag{9}$$

depends on the internal magnetic field

$$H_\text{i} = H_0 - H_\text{d} = H_0 - N_\text{d} M_0 > 0 \tag{10}$$

and on the micromagnetic exchange length of the field

$$l_\text{H}(H_\text{i}) = \sqrt{\frac{2A}{\mu_0 M_0 H_\text{i}}} \tag{11}$$

(M_0: saturation magnetization; A: exchange-stiffness parameter; $H_\text{d} = N_\text{d} M_0$: demagnetizing field; $0 \leqslant N_\text{d} \leqslant 1$: demagnetizing factor; $\mu_0 = 4\pi\,10^{-7}$ Tm/A). Note that $H_0 \gg H_\text{d}$ in the approach-to-saturation regime. The θ dependence of R_H and R_M arises essentially as a consequence of the magnetodipolar interaction. Depending on the values of q and H_i, a variety of angular anisotropies may be seen on a two-dimensional position-sensitive detector [16].

The effective magnetic field H_{eff} [Eq. (9)] consists of a contribution due to the internal field H_i and of the exchange field $2Aq^2/(\mu_0 M_0)$. An increase of H_i increases the effective field only at the smallest q values, whereas H_{eff} at the larger q is always very large ($\sim$10–100 T) and independent of H_i [16]. The latter statement may be seen as a manifestation of the fact that exchange forces tend to dominate on small length scales [42]. The role of H_{eff} is to suppress the high-q Fourier components of the magnetization, which correspond to sharp real-space fluctuations. On the other hand, long-range magnetization fluctuations, at small q, are effectively suppressed when H_i is increased.

By assuming the functions $\widetilde{N}$, $\widetilde{M}_z$, and $\widetilde{\mathbf{H}}_\text{p}$ to depend only on the magnitude $q = |\mathbf{q}|$ of the scattering vector, one can perform an azimuthal average of Eq. (1), i.e., $1/(2\pi)\int_0^{2\pi}(\ldots)d\theta$. The resulting expressions for the response functions then read

$$R_\text{H}(q, H_\text{i}) = \frac{p^2}{4}\left(2 + \frac{1}{\sqrt{1+p}}\right) \tag{12}$$

and

$$R_\text{M}(q, H_\text{i}) = \frac{\sqrt{1+p} - 1}{2}, \tag{13}$$

so that the azimuthally averaged total nuclear and magnetic SANS cross section can be written as

$$\begin{aligned}\frac{d\Sigma}{d\Omega}(q, H_\text{i}) &= \frac{d\Sigma_\text{res}}{d\Omega}(q) + \frac{d\Sigma_\text{M}}{d\Omega}(q, H_\text{i}) \\ &= \frac{d\Sigma_\text{res}}{d\Omega}(q) + S_\text{H}(q)\, R_\text{H}(q, H_\text{i}) \\ &\quad + S_\text{M}(q)\, R_\text{M}(q, H_\text{i}),\end{aligned} \tag{14}$$

where

$$\frac{d\Sigma_\text{res}}{d\Omega}(q) = \frac{8\pi^3}{V}\left(|\widetilde{N}(q)|^2 + \frac{1}{2} b_\text{H}^2\, |\widetilde{M}_z(q)|^2\right). \tag{15}$$

For materials exhibiting a uniform saturation magnetization (e.g., single-phase materials), the magnetostatic scattering contribution $S_\text{M} R_\text{M}$ to $d\Sigma_\text{M}/d\Omega$ [compare Eq. (3)] is expected to be much smaller than the anisotropy-field related term $S_\text{H} R_\text{H}$ (compare, e.g., Fig. 23 in Ref. [43]).

We emphasize that the micromagnetic theory behind the *MuMag2022* software results in an analytical expression for the two-dimensional SANS cross section as a function of the magnitude q and the orientation θ of the scattering vector $\mathbf{q}$. These analytical expressions can be azimuthally averaged over the full angular detector range 2π (or any other range) and compared to correspondingly averaged experimental SANS data, in other words, it is not required that the experimental input SANS data are isotropic. Equation (14) is the central expression that is used here to analyze the 1D SANS data. The free parameters are $d\Sigma_\text{res}/d\Omega$, S_H, S_M, and the exchange constant A in the expressions for R_H and R_M. Numerical integration of the obtained $S_\text{H}(q)$ and $S_\text{M}(q)$ over the whole $\mathbf{q}$ space, i.e.,

$$\langle|\mathbf{H}_\text{p}|^2\rangle = \frac{1}{2\pi^2 b_\text{H}^2}\int_0^\infty S_\text{H}(q)\, q^2\, dq, \tag{16}$$

$$\langle|M_z|^2\rangle = \frac{1}{2\pi^2 b_\text{H}^2}\int_0^\infty S_\text{M}(q)\, q^2\, dq, \tag{17}$$

yields, respectively, the mean-square anisotropy field $\langle|\mathbf{H}_\text{p}|^2\rangle$ and the mean-square longitudinal magnetization fluctuation $\langle|M_z|^2\rangle$ [16]. Since experimental data for S_H and S_M are only available within a finite range of momentum transfers between q_min and q_max, one can only obtain rough lower bounds for these quantities. Therefore, the numerical integrations in Eqs. (16) and (17) are carried out for $q_\text{min} \leqslant q \leqslant q_\text{max}$; q_min denotes the first experimental data point, while $q_\text{max} \cong [\mu_0 M_0 H_\text{max}/(2A)]^{1/2}$ can be estimated based on the value of the maximum applied magnetic field H_max. For $q \gtrsim q_\text{max}$, the reliable separation of the spin-misalignment ($S_\text{H} R_\text{H} + S_\text{M} R_\text{M}$) and residual scattering ($d\Sigma_\text{res}/d\Omega$) is difficult (since then one attempts to fit a straight line to a constant), and the micromagnetic analysis should therefore be restricted to $q \lesssim q_\text{max}$; see Ref. [36] for further details on the data analysis and the fit procedure.

IV. RESULTS AND DISCUSSION

Figure 3 displays, for the three alloy systems studied, the two-dimensional purely magnetic SANS cross section $d\Sigma_\text{M}/d\Omega$ at selected applied magnetic fields, obtained after subtracting the respective nuclear and magnetic scattering at a saturating field of 9 T. The Appendix features a summary of the neutron data for the total $d\Sigma/d\Omega$ and $d\Sigma_\text{M}/d\Omega$ at a number of fields and for all three sample-to-detector distances. As discussed in the previous section, the subtraction procedure approximately removes the nuclear and (longitudinal) magnetic scattering due to a saturated microstructure and in this way highlights the magnetic scattering that is related to the magnetic interactions. With decreasing field, we note in Fig. 3 (and in the corresponding $d\Sigma_\text{M}/d\Omega$ data sets in the Appendix) the appearance of a pronounced angular anisotropy in $d\Sigma_\text{M}/d\Omega$ with maxima roughly along the diagonals of the detector. Comparison to Eqs. (3) and (7) suggests that this so-called clover-leaf anisotropy is related

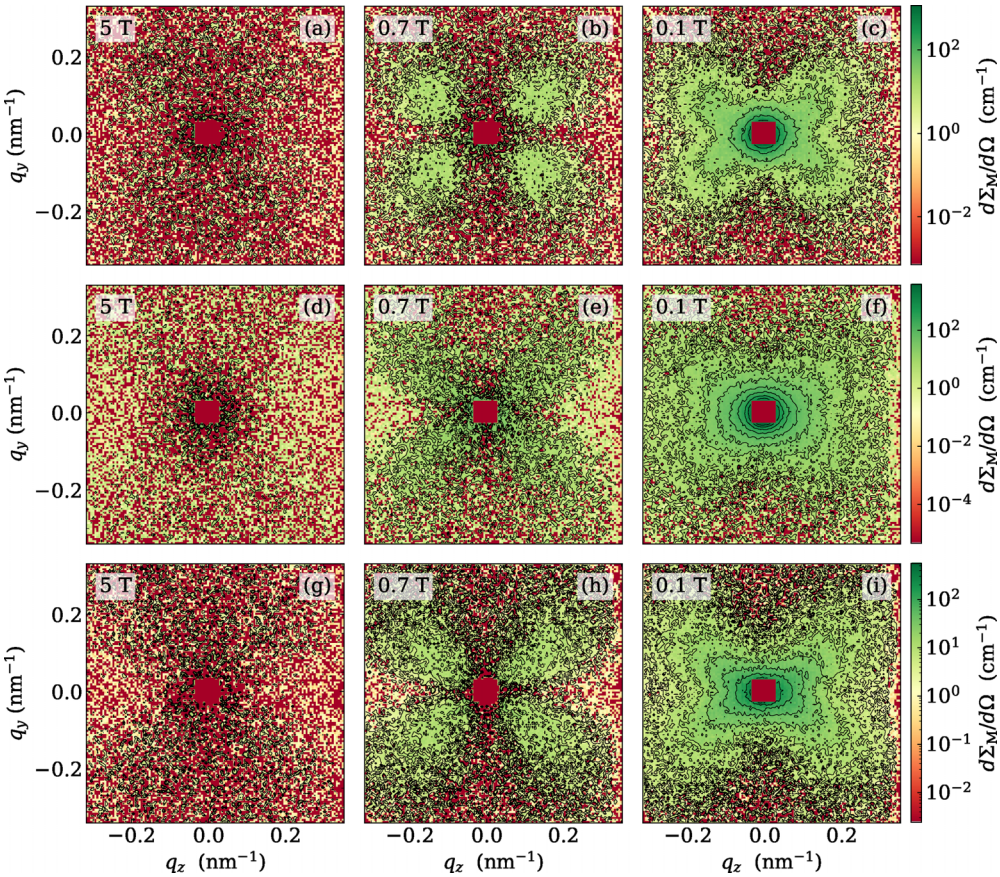

FIG. 3. Magnetic SANS cross sections of Nanoperm alloys (sample-to-detector distance: 18 m) (logarithmic color scale). The data were obtained by subtracting the respective total (nuclear and magnetic) SANS intensity at 9 T from the measurements at the lower fields (indicated in the top left corner of each subfigure). $\mathbf{H}_0 \parallel \mathbf{e}_z$ is horizontal. (a)–(c) $Fe_{87}B_{13}$; (d)–(f) $Fe_{85}Nb_6B_9$; (g)–(i) $Fe_{80}Nb_6B_{14}$.

to the magnetostatic scattering term $S_M R_M$ rather than to the anisotropy-field related contribution $S_H R_H$. As we will see below, the clover leaf pattern is very likely related to nanoscale jumps in the magnetization magnitude at internal particle-matrix interfaces, which give rise to local magnetostatic stray fields causing spin disorder. Similar angular anisotropies have also been reported for other compounds [15,18,32,44–48].

Figure 4 shows the results of the micromagnetic SANS data analysis for the azimuthally averaged total unpolarized SANS cross section $d\Sigma/d\Omega$. The analysis, carried out using the *MuMag2022* software [36], has been restricted to applied fields larger than about 0.1 T, where the normalized magnetization is larger than ∼95 %, so that all the Nanoperm samples are in the approach-to-saturation regime (compare Fig. 2). It is seen that the computed cross sections based on the micromagnetic SANS theory [solid lines, Eq. (14)] very well reproduce the experimental data. As is typical for spin-misalignment scattering of bulk ferromagnets, the largest field dependence of $d\Sigma/d\Omega$ appears at the smallest momentum transfers, where also the clover-leaf pattern in the 2D data is most pronounced. The SANS data analysis has been restricted to $q \lesssim q_{max} = 0.6\,\mathrm{nm}^{-1}$, since the reliable separation of the spin misalignment ($S_H R_H + S_M R_M$) and residual scattering ($d\Sigma_{res}/d\Omega$) is difficult for $q \gtrsim q_{max}$. This explains the increase of the uncertainty values in the data for S_H and S_M in Fig. 4 with increasing momentum transfer q.

The fit analysis provides the values of the exchange-stiffness constant A as well as the average anisotropy field $\sqrt{\langle|\mathbf{H}_p|^2\rangle}$ and magnetostatic field $\sqrt{\langle|M_z|^2\rangle}$ (see Table II). We re-emphasize that the values for $\sqrt{\langle|\mathbf{H}_p|^2\rangle}$ and $\sqrt{\langle|M_z|^2\rangle}$ are lower bounds, since the experimental data for S_H and S_M are only available within a finite range of momentum transfers between q_{min} and q_{max}. It is also important to mention that these values represent effective values that are averaged over particle and matrix phases. The A values are subsequently used to calculate the micromagnetic exchange lengths l_H [Eq. (11)], and the field dependence of the micromagnetic correlation

TABLE II. Results of the micromagnetic SANS data analysis for the exchange-stiffness constant (A), mean-square anisotropy ($\sqrt{\langle|\mathbf{H}_p|^2\rangle}$), and mean-square magnetostatic field ($\sqrt{\langle|M_z|^2\rangle}$).

Alloy	A (pJ/m)	$\mu_0\sqrt{\langle\|\mathbf{H}_p\|^2\rangle}$ (mT)	$\mu_0\sqrt{\langle\|M_z\|^2\rangle}$ (mT)
$Fe_{87}B_{13}$	18.5 ± 0.7	83	207
$Fe_{85}Nb_6B_9$	14.6 ± 0.2	45	326
$Fe_{80}Nb_6B_{14}$	10.9 ± 0.2	132	325

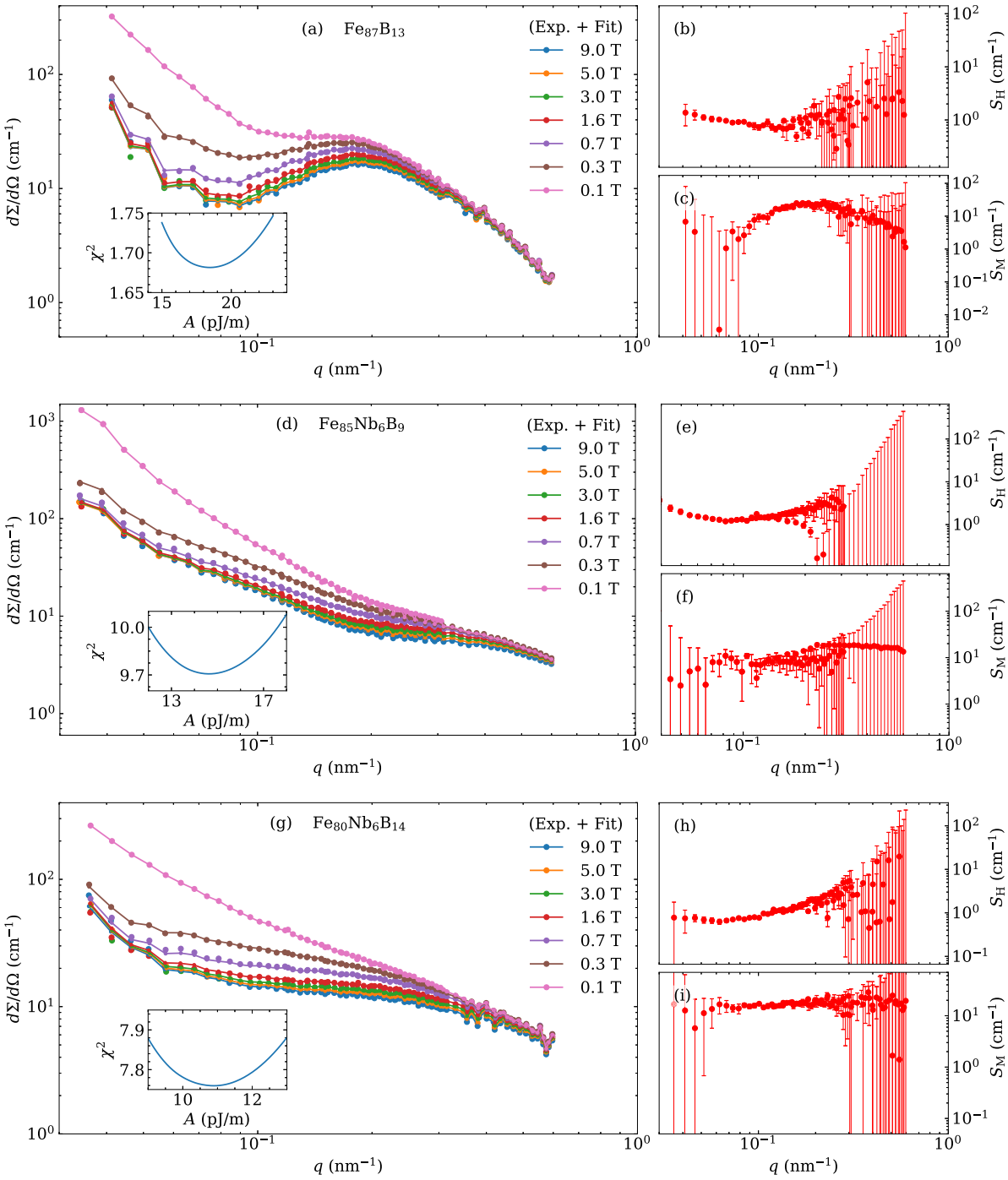

FIG. 4. Results of the micromagnetic SANS data analysis for the azimuthally averaged total unpolarized SANS cross section. (a)–(c) $Fe_{87}B_{13}$; (d)–(f) $Fe_{85}Nb_6B_9$; (g)–(i) $Fe_{80}Nb_6B_{14}$. In (a), (d), and (g), the dots denote the respective experimental data and the solid lines connect the computed cross section values at the discrete q and H_i using Eq. (14). Insets in (a), (d), and (g) show the goodness of fit, χ^2, for a range of exchange-stiffness constants A. Subfigures (b), (c); (e), (f); and (h), (i) display the respective results for the anisotropy-field (S_H) and magnetostatic (S_M) scattering functions. The fit analysis was restricted to $q \lesssim q_{max} = 0.6\,nm^{-1}$ for all samples.

length

$$l_C(H_i) = D + l_H(H_i) = D + \sqrt{\frac{2A}{\mu_0 M_0 H_i}}, \qquad (18)$$

where D is the average particle size, is depicted in Fig. 5. This length scale can be interpreted as the characteristic size regime over which perturbations in the spin structure are effectively mediated by the exchange interaction [49–51]. It is seen that the l_C for all three samples exhibit a similar field variation

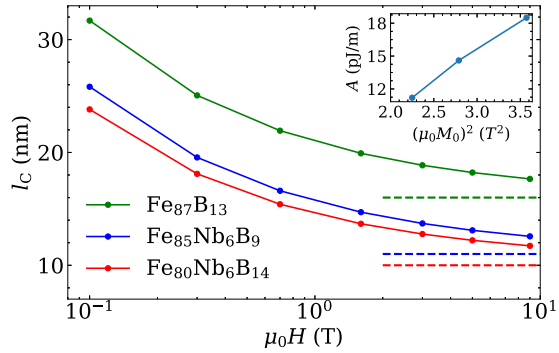

FIG. 5. Field variation of the correlation length l_C [Eq. (18)] (semilog scale). The dashed lines indicate the average particle size D (compare Table I). Inset: Plot of A versus $(\mu_0 M_0)^2$.

with sizes ranging between about 10–35 nm. The behavior of the exchange constant appears to be in line with the expected $A \propto M_0^2$ scaling (see the inset in Fig. 5) [52].

Previously, we have utilized the present micromagnetic SANS data analysis to estimate the volume-averaged exchange-stiffness constants in a number of Fe-based nanocrystalline alloys. For $Fe_{89}Zr_7B_3Cu$, $(Fe_{0.985}Co_{0.015})_{90}Zr_7B_3$ [40], and $(Fe_{0.7}Ni_{0.3})_{86}B_{14}$ [32], we have found, respectively, $A = 3.1\,\mathrm{pJ/m}$, $A = 4.7\,\mathrm{pJ/m}$, and $A = 10.0\,\mathrm{pJ/m}$. The present values in Table II are somewhat larger than these, which might be surprising in view of the fact that a typical A value for these types of alloys is often taken as $\sim 10.0\,\mathrm{pJ/m}$ (e.g., Ref. [3]). However, it must be emphasized that (i) the volume-averaged A value may depend on the composition and on the microstructure (e.g., the heat treatment) and that (ii) there exists a certain scatter in the values depending on the used experimental technique. To classify our experimental data we provide the following consideration. The value of A at a given temperature can be computed based on the experimental value for the spin-wave stiffness constant $\mathcal{D}$, according to [53]

$$\mathcal{D} = \frac{2Ag\mu_B}{M_0}, \tag{19}$$

where g is the Landé factor and μ_B the Bohr magneton. The parameter $\mathcal{D}$ can, e.g., be determined from inelastic neutron scattering, magnetization, or spin-wave resonance experiments. Using the room temperature value of $\mathcal{D} = 281\,\mathrm{meV\,Å^2}$ for single crystalline Fe, obtained by triple-axis neutron spectroscopy [54], $g = 2.10$ and $\mu_0 M_0 = 2.15\,\mathrm{T}$ [55], one obtains $A \cong 19.8\,\mathrm{pJ/m}$. This value for pure Fe may be seen as an upper bound to our A values obtained on Fe-based alloys.

The analysis of the azimuthally averaged SANS data also provides the residual SANS cross section $d\Sigma_{res}/d\Omega$, which represents the nuclear and longitudinal magnetic scattering at saturation. The q dependence of the $d\Sigma_{res}/d\Omega$ for all three Nanoperm samples is compared in Fig. 6 with the corresponding small-angle x-ray scattering (SAXS) cross sections. The shown $d\Sigma_{res}/d\Omega$ have been scaled by constant factors to closely match the SAXS data. It can be seen that for $Fe_{87}B_{13}$ [Fig. 6(a)] the $d\Sigma_{res}/d\Omega$ matches very well with its SAXS cross section over the entire range of scattering

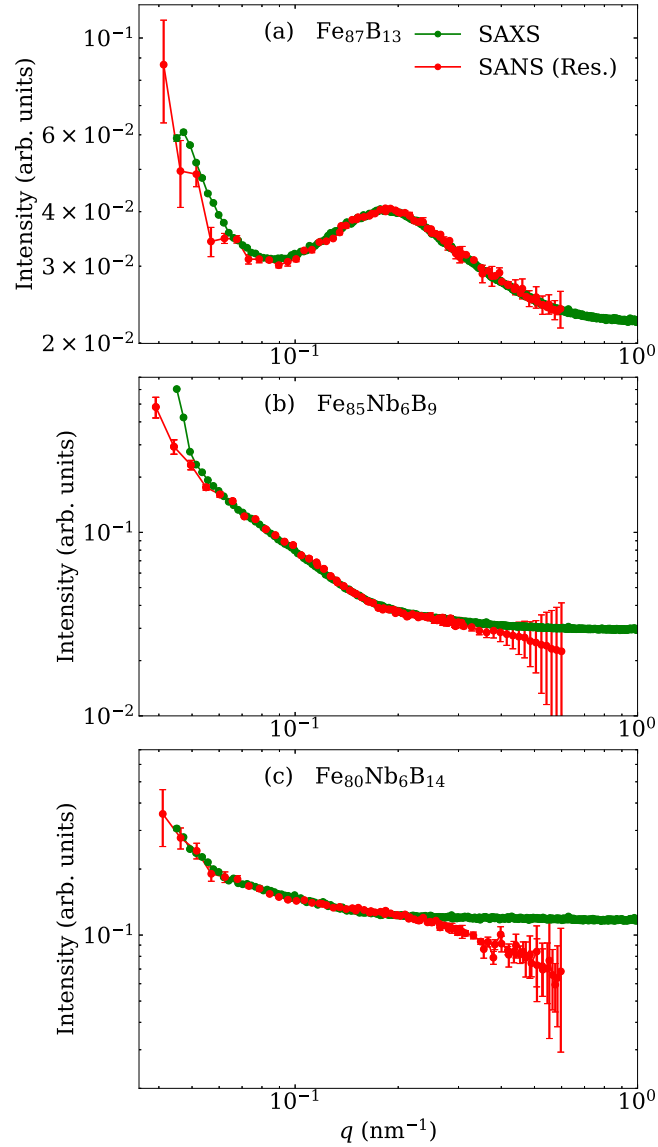

FIG. 6. (a)–(c) Comparison of the residual SANS cross sections $d\Sigma_{res}/d\Omega$ of the three Nanoperm alloys (obtained from the micromagnetic neutron data analysis) with the respective SAXS signal (see insets) (log-log scale).

vectors. The peak at $q_{max} \cong 0.185\,\mathrm{nm^{-1}}$ (corresponding to $2\pi/q_{max} \cong 34\,\mathrm{nm}$) is also observable in SAXS and reproduced by the micromagnetic SANS data analysis as well. The data in Fig. 6(a) suggest that the nuclear and magnetic microstructure at saturation are "congruent", i.e., the structural features giving rise to the SAXS signal have essentially the same size, shape, and arrangement as the objects that are at the origin of $d\Sigma_{res}/d\Omega$. For $Fe_{85}Nb_6B_9$ and $Fe_{80}Nb_6B_{14}$ [Figs. 6(b) and 6(c)], both cross sections agree reasonably only at low and intermediate momentum transfers. This might be explained by the fact that the micromagnetic SANS data analysis becomes progressively more difficult at large q (at least for these two samples), when the SANS cross section is independent of the field (compare the error bars in Fig. 6).

Uniaxial neutron polarization analysis could in principle also be carried out on the Nanoperm samples since the magnetic scattering of interest is at low momentum transfers q and should therefore not be obscured by the scattering from the ^{3}He analyzer cell (at the larger q). In fact, similar formulas for the spin-flip SANS cross section, based on micromagnetic theory, have been worked out for this case (see Ref. [56]). However, polarization analysis experiments are very time consuming (due to the required spin-leakage correction) and can hardly be done on a series of samples and over a range of fields (as is done here). Moreover, there will be no significant gain of information in a polarized SANS experiment as compared to an unpolarized one since the micromagnetic neutron data analysis will work in the very same way (as demonstrated in [56]). The only (minor) difference would be that the nuclear coherent "background" signal is not present in the spin-flip SANS cross section, so that the individual magnetic scattering contributions (such as the clover-leaf pattern) will directly become visible, without the necessity to subtract the total nuclear and magnetic scattering at saturation (as is done here in an unpolarized experiment).

V. SUMMARY AND CONCLUSION

We have conducted a combined SANS and SAXS study on a series of nanocrystalline two-phase Nanoperm alloys ($Fe_{87}B_{13}$, $Fe_{85}Nb_6B_9$, $Fe_{80}Nb_6B_{14}$). The SANS data can be very well described by micromagnetic SANS theory and yield values for the exchange-stiffness constants as well as estimates for the average anisotropy and magnetostatic fields. A distinct clover-leaf-shaped angular anisotropy in the magnetic SANS cross section strongly suggests that the magnetic scattering in these compounds predominantly stems from the magnetodipolar stray fields decorating the nanocrystals. This is in line with the observation that the average magnetostatic fields due to spatial variations in the longitudinal magnetization are much larger than the anisotropy fields. The obtained exchange-stiffness constants allowed us to draw conclusions on the field dependence of the micromagnetic exchange length, which is a measure for the size regime ($\sim$10–35 nm) over which perturbations in the spin structure are effectively mediated by the exchange interaction. The nuclear and magnetic residual SANS cross sections, as obtained from the micromagnetic SANS data analysis, closely resemble the purely structural SAXS signal, providing further support for the validity of the micromagnetic SANS theory. Based on the neutron results we can state that the magnetic microstructure of the studied Nanoperm alloys is governed by static nanometer-scale long-wavelength magnetization fluctuations that have their origin in a highly nonuniform saturation magnetization profile $M_s(\mathbf{r})$. From an application point of view, it might be beneficial to reduce the inhomogeneity in $M_s(\mathbf{r})$, e.g., via the engineering of nanocrystallites that have a saturation magnetization equal or close to the matrix material, in this way reducing large jumps in M_s.

ACKNOWLEDGMENTS

The authors acknowledge the Swiss spallation neutron source at the Paul Scherrer Institute for the provision of neutron beam time at the SANS-I instrument. They are also thankful to H. Huang for preparing the ribbon samples. M.P.A. acknowledges financial support from the National Research Fund of Luxembourg (AFR Grant No. 15639149).

APPENDIX: OVERVIEW OF SANS RESULTS FOR $d\Sigma/d\Omega$ AND $d\Sigma_M/d\Omega$

In this Appendix we display additional results (Figs. 7–12) for the two-dimensional total (nuclear and magnetic) SANS cross section $d\Sigma/d\Omega$ and for the purely magnetic SANS cross section $d\Sigma_M/d\Omega$ of the Nanoperm alloys.

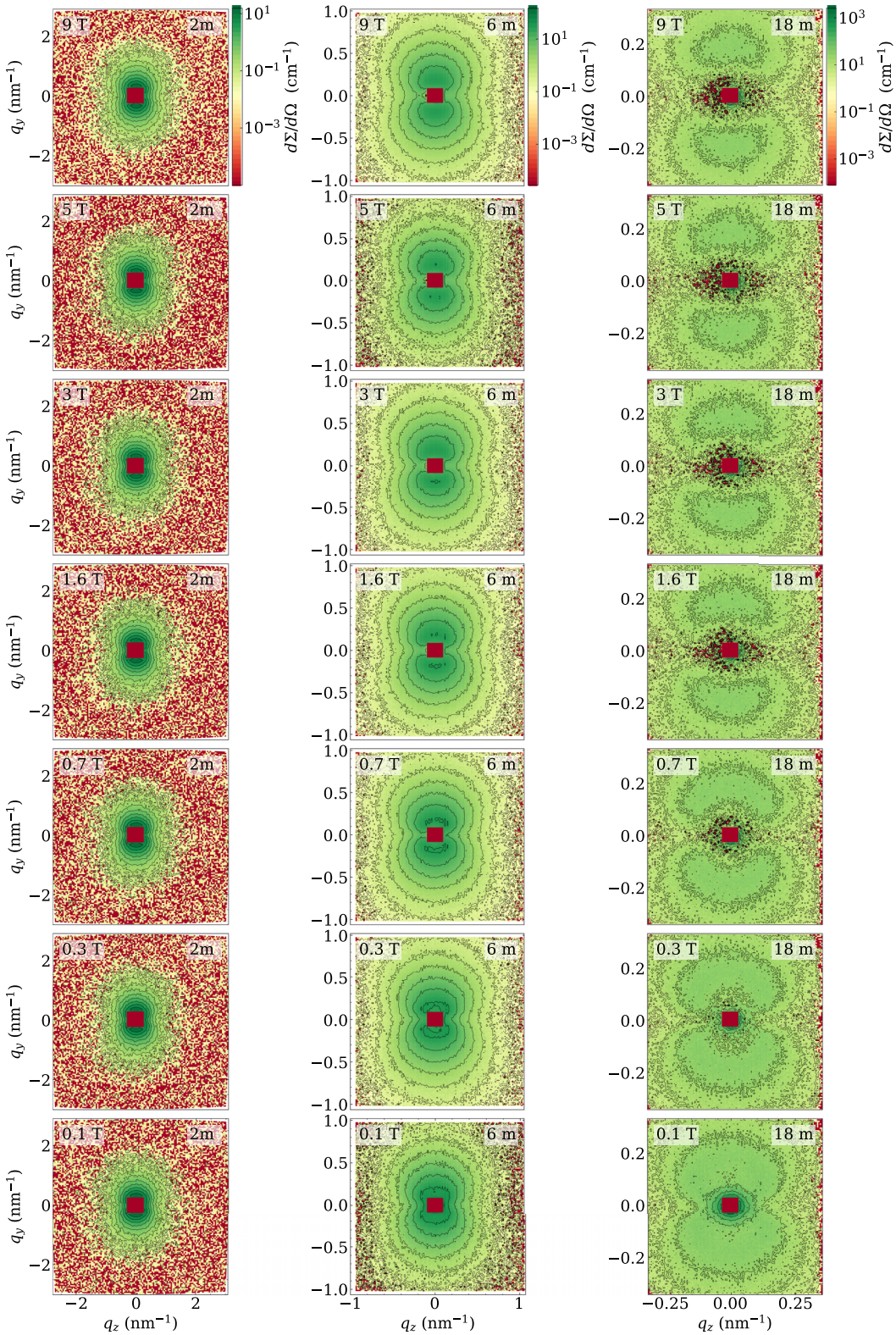

FIG. 7. Total nuclear and magnetic SANS cross section $d\Sigma/d\Omega$ of $Fe_{87}B_{13}$ alloy at selected applied magnetic fields (see insets) (logarithmic color scale). The sample-to-detector distance varies from the left to the right column (2 m, 6 m, 18 m).

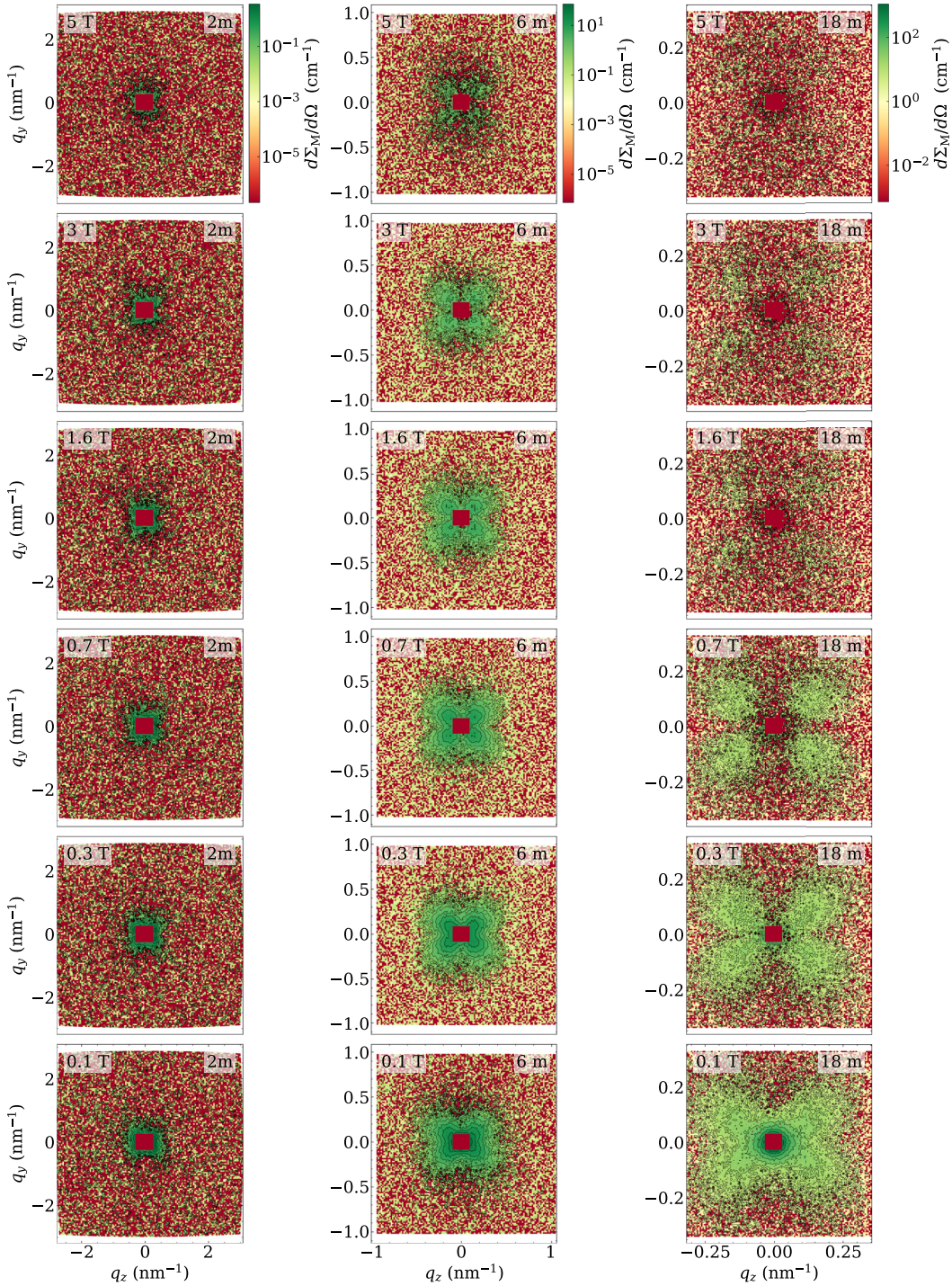

FIG. 8. Magnetic SANS cross section $d\Sigma_M/d\Omega$ of $Fe_{87}B_{13}$ alloy at selected applied magnetic fields (see insets) (logarithmic color scale). The nuclear and magnetic scattering at 9 T (saturation) has been subtracted from each data set.

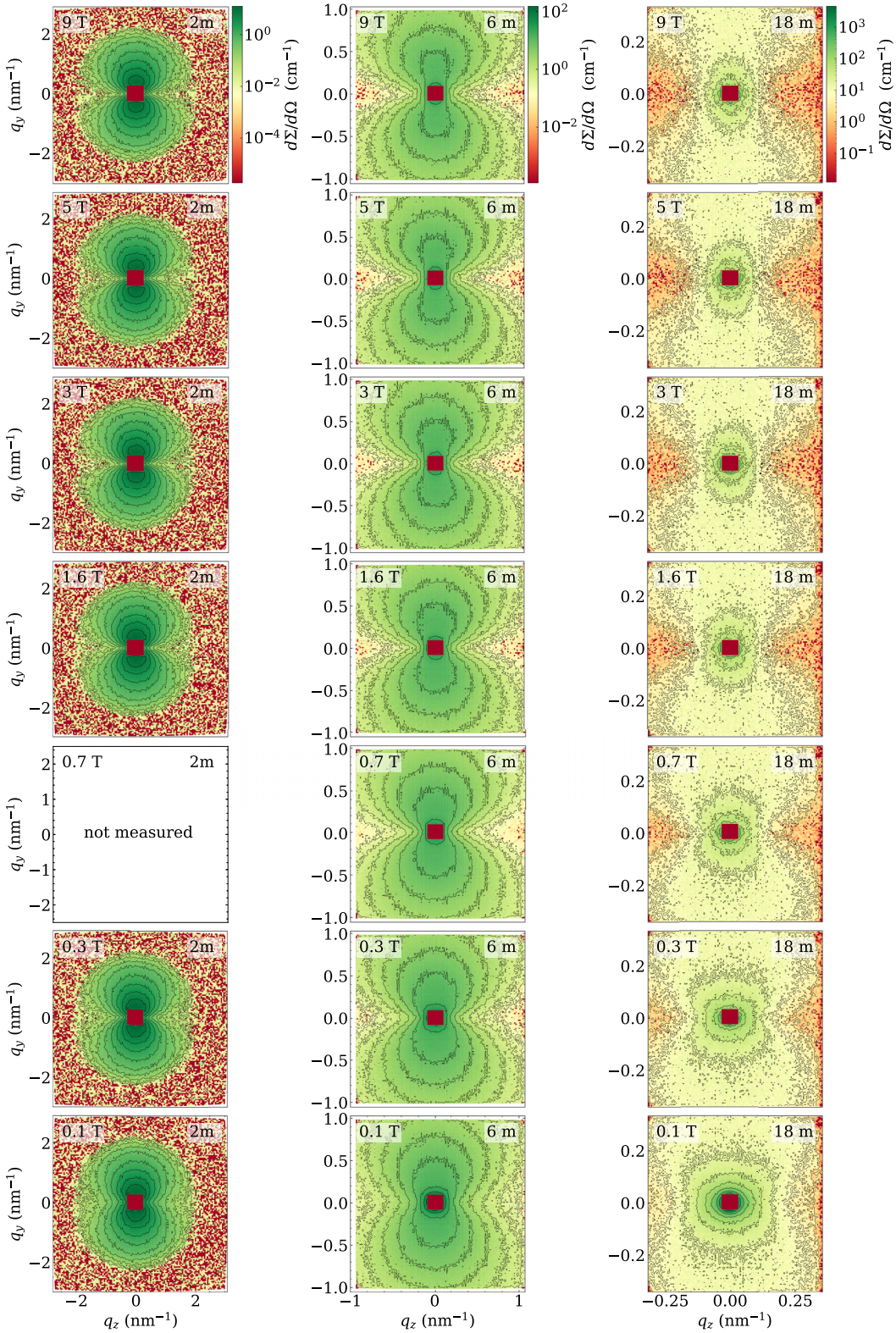

FIG. 9. Total nuclear and magnetic SANS cross section $d\Sigma/d\Omega$ of $Fe_{85}Nb_6B_9$ alloy at selected applied magnetic fields (see insets) (logarithmic color scale).

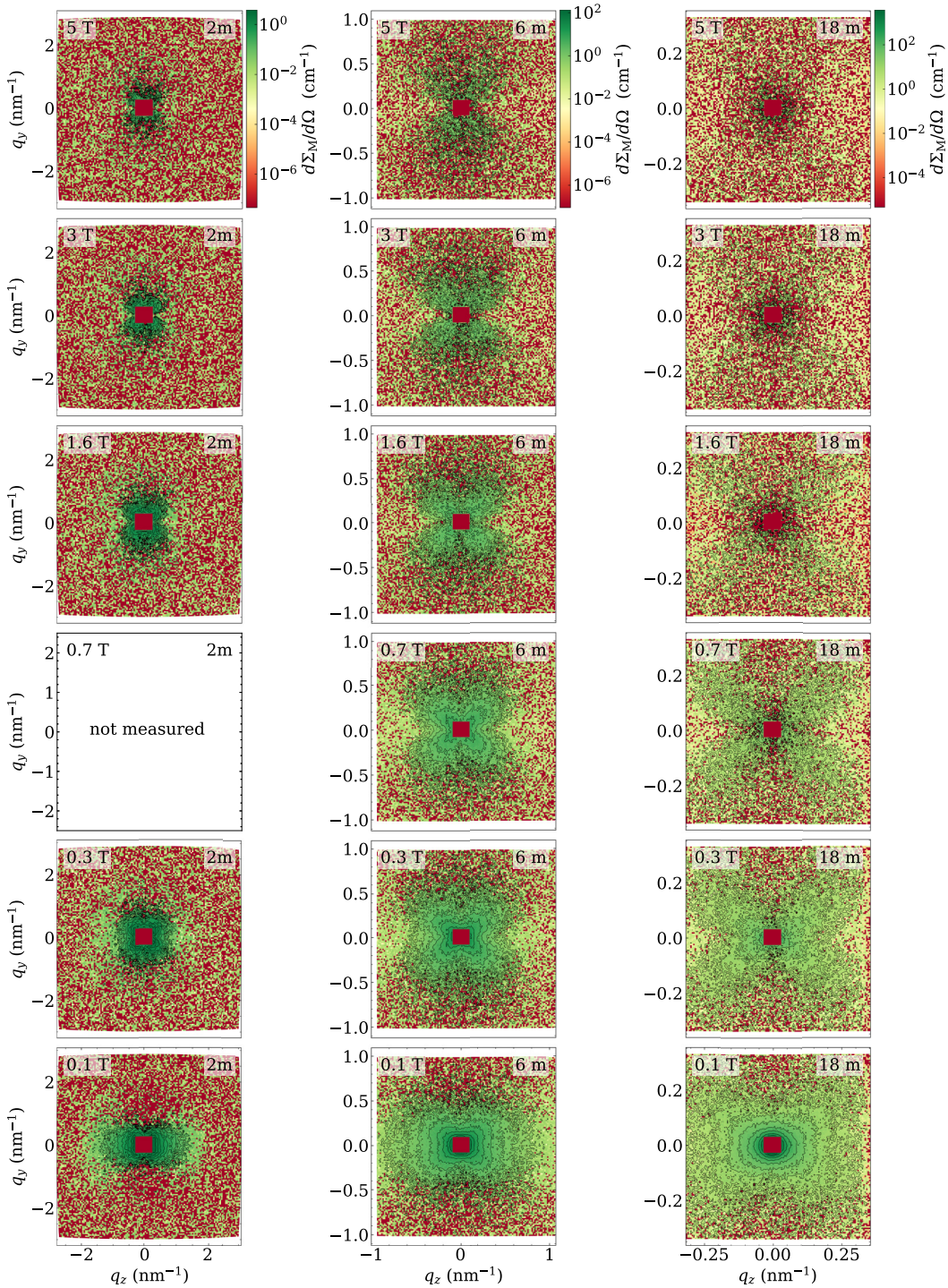

FIG. 10. Magnetic SANS cross section $d\Sigma_M/d\Omega$ of $Fe_{85}Nb_6B_9$ alloy at selected applied magnetic fields (see insets) (logarithmic color scale). The nuclear and magnetic scattering at 9 T (saturation) has been subtracted from each data set.

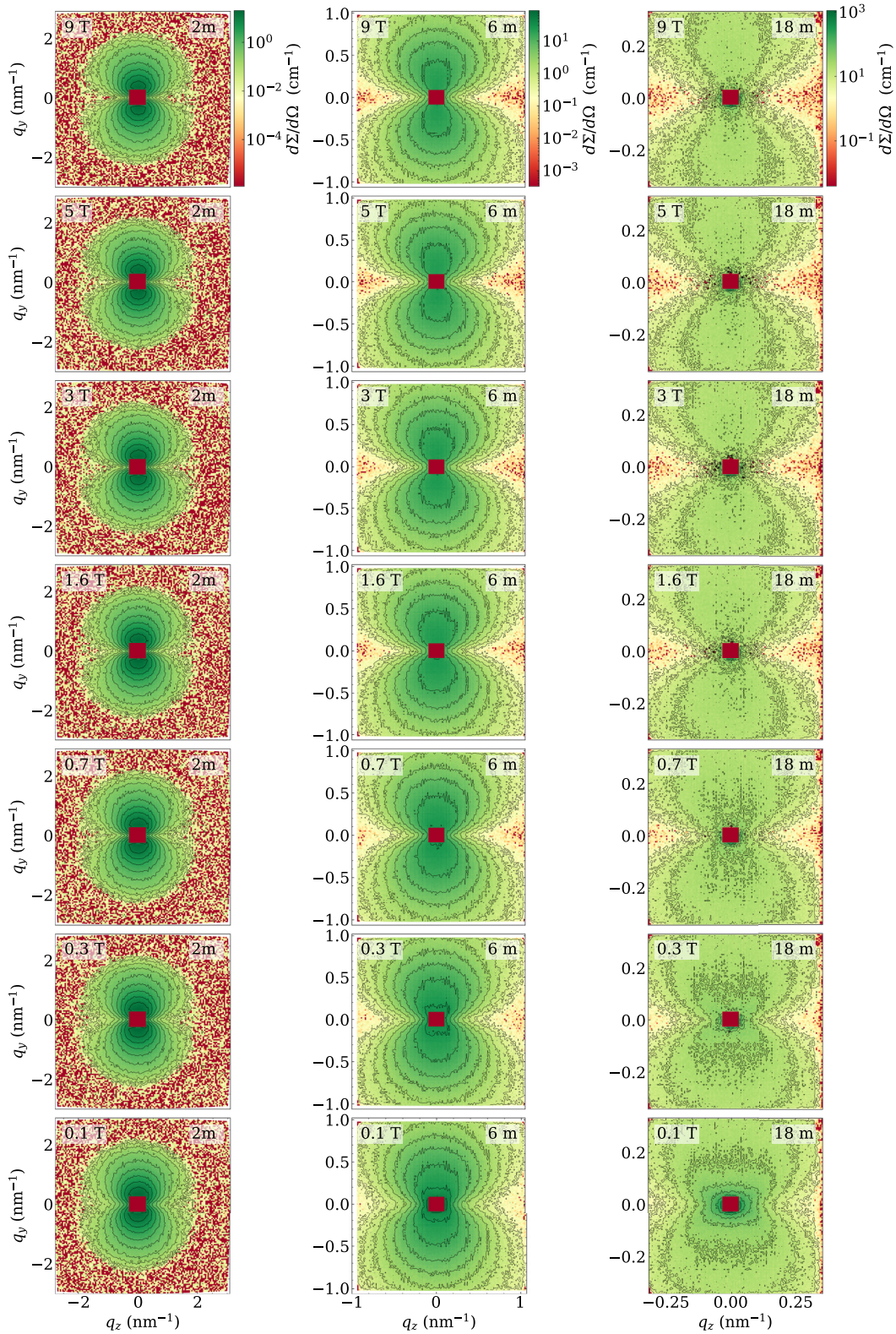

FIG. 11. Total nuclear and magnetic SANS cross section $d\Sigma/d\Omega$ of $Fe_{80}Nb_6B_{14}$ alloy at selected applied magnetic fields (see insets) (logarithmic color scale).

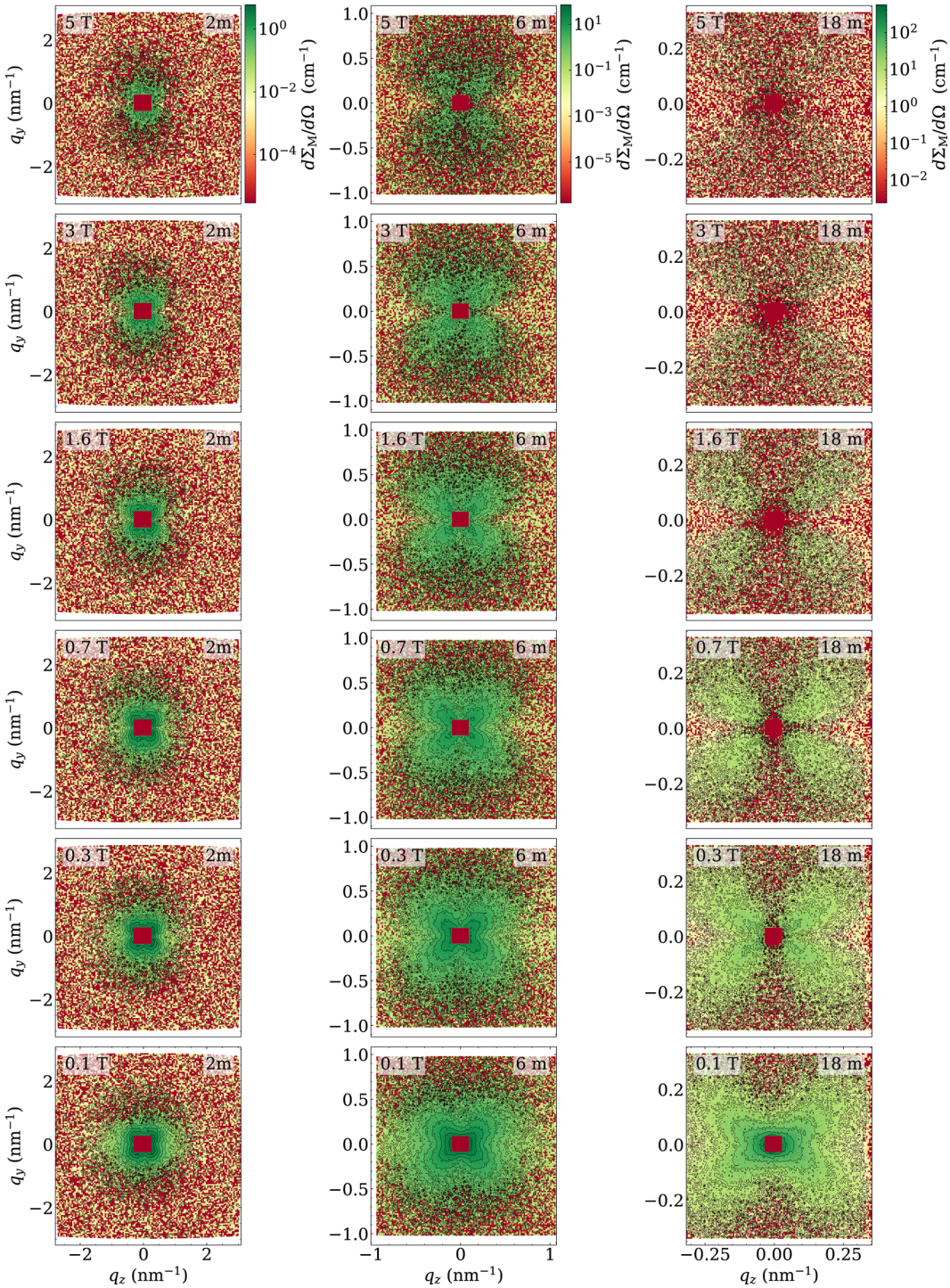

FIG. 12. Magnetic SANS cross section $d\Sigma_M/d\Omega$ of $Fe_{80}Nb_6B_{14}$ alloy at selected applied magnetic fields (see insets) (logarithmic color scale). The nuclear and magnetic scattering at 9 T (saturation) has been subtracted from each data set.

[1] Y. Yoshizawa, S. Oguma, and K. Yamauchi, New Fe-based soft magnetic alloys composed of ultrafine grain structure, J. Appl. Phys. **64**, 6044 (1988).

[2] G. Herzer, Grain size dependence of coercivity and permeability in nanocrystalline ferromagnets, IEEE Trans. Magn. **26**, 1397 (1990).

[3] G. Herzer, Nanocrystalline soft magnetic alloys, in *Handbook of Magnetic Materials*, edited by K. H. J. Buschow (Elsevier, Amsterdam, 1997), Vol. 10, pp. 415–462.

[4] K. Suzuki, Nanocrystalline soft magnetic materials: A decade of alloy development, Materials Science Forum **312**, 521 (1999).

[5] K. Suzuki and G. Herzer, Soft magnetic nanostructures and applications, in *Advanced Magnetic Nanostructures*, edited by D. Sellmyer and R. Skomski (Springer-Verlag, New York, 2006), pp. 365–401.

[6] O. Gutfleisch, M. A. Willard, E. Brück, C. H. Chen, S. Sankar, and J. P. Liu, Magnetic materials and devices for the 21st century: stronger, lighter, and more energy efficient, Adv. Mater. **23**, 821 (2011).

[7] A. Urata, M. Yamaki, M. Takahashi, K. Okamoto, H. Matsumoto, S. Yoshida, and A. Makino, Low core loss of non-Si quaternary $Fe_{83.3}B_8P_8Cu_{0.7}$ nanocrystalline alloy with high B_s of 1.7 T, J. Appl. Phys. **111**, 07A335 (2012).

[8] G. Herzer, Modern soft magnets: Amorphous and nanocrystalline materials, Acta Mater. **61**, 718 (2013).

[9] M. Hasiak, M. Miglierini, M. Łukiewski, and J. Kaleta, Impact of microstructure upon soft magnetic properties of cobalt-doped metallic glasses, IEEE Trans. Magn. **50**, 1 (2014).

[10] M. Hasiak, A. Laszcz, A. Zak, and J. Kaleta, Microstructure and magnetic properties of Nanoperm-type soft magnetic material, Acta Phys. Pol. A **135**, 284 (2019).

[11] B. S. Ram, A. Paul, and S. Kulkarni, Soft magnetic materials and their applications in transformers, J. Magn. Magn. Mater. **537**, 168210 (2021).

[12] H. Huang, R. Parsons, H. Tsukahara, M. Yano, T. Shoji, A. Kato, K. Ono, and K. Suzuki, Effect of grain size on the core loss of nanocrystalline $Fe_{86}B_{13}Cu_1$ prepared by ultra-rapid annealing, AIP Adv. **13**, 025304 (2023).

[13] H. Tsukahara, H. Imamura, C. Mitsumata, K. Suzuki, and K. Ono, Role of magnetostriction on power losses in nanocrystalline soft magnets, NPG Asia Mater. **14**, 44 (2022).

[14] H. Huang, H. Tsukahara, A. Kato, K. Ono, and K. Suzuki, Origin of excess core loss in amorphous and nanocrystalline soft magnetic materials, Phys. Rev. B **109**, 104408 (2024).

[15] S. Mühlbauer, D. Honecker, É. A. Périgo, F. Bergner, S. Disch, A. Heinemann, S. Erokhin, D. Berkov, C. Leighton, M. R. Eskildsen *et al.*, Magnetic small-angle neutron scattering, Rev. Mod. Phys. **91**, 015004 (2019).

[16] A. Michels, *Magnetic Small-Angle Neutron Scattering: A Probe for Mesoscale Magnetism Analysis* (Oxford University Press, Oxford, 2021).

[17] A. Michels, R. N. Viswanath, and J. Weissmüller, Domain formation and long-range spin disorder in Vitroperm, Europhys. Lett. **64**, 43 (2003).

[18] A. Michels, C. Vecchini, O. Moze, K. Suzuki, P. K. Pranzas, J. Kohlbrecher, and J. Weissmüller, Dipolar correlations in a nanocomposite: A neutron scattering study of Nanoperm $Fe_{89}Zr_7B_3Cu$, Phys. Rev. B **74**, 134407 (2006).

[19] N. Ito, A. Michels, J. Kohlbrecher, J. S. Garitaonandia, K. Suzuki, and J. D. Cashion, Effect of magnetic field annealing on the soft magnetic properties of nanocrystalline materials, J. Magn. Magn. Mater. **316**, 458 (2007).

[20] C. Heintze, F. Bergner, A. Ulbricht, and H. Eckerlebe, The microstructure of neutron-irradiated Fe–Cr alloys: A small-angle neutron scattering study, J. Nucl. Mater. **409**, 106 (2011).

[21] K. P. Bhatti, S. El-Khatib, V. Srivastava, R. D. James, and C. Leighton, Small-angle neutron scattering study of magnetic ordering and inhomogeneity across the martensitic phase transformation in $Ni_{50-x}Co_xMn_{40}Sn_{10}$ alloys, Phys. Rev. B **85**, 134450 (2012).

[22] F. Bergner, C. Pareige, V. Kuksenko, L. Malerba, P. Pareige, A. Ulbricht, and A. Wagner, Critical assessment of Cr-rich precipitates in neutron-irradiated Fe-12at%Cr: Comparison of SANS and APT, J. Nucl. Mater. **442**, 463 (2013).

[23] R. Pareja, P. Parente, A. Muñoz, A. Radulescu, and V. de Castro, Small-angle neutron scattering study of the nano-sized features in an oxide dispersion-strengthened Fe12Cr alloy, Philos. Mag. **95**, 2450 (2015).

[24] A. J. Grutter, K. L. Krycka, E. V. Tartakovskaya, J. A. Borchers, K. S. M. Reddy, E. Ortega, A. Ponce, and B. J. H. Stadler, Complex three-dimensional magnetic ordering in segmented nanowire arrays, ACS Nano **11**, 8311 (2017).

[25] S. Shu, B. D. Wirth, P. B. Wells, D. D. Morgan, and G. R. Odette, Multi-technique characterization of the precipitates in thermally aged and neutron irradiated Fe-Cu and Fe-Cu-Mn model alloys: Atom probe tomography reconstruction implications, Acta Mater. **146**, 237 (2018).

[26] P. Bender, E. Wetterskog, D. Honecker, J. Fock, C. Frandsen, C. Moerland, L. K. Bogart, O. Posth, W. Szczerba, H. Gavilán *et al.*, Dipolar-coupled moment correlations in clusters of magnetic nanoparticles, Phys. Rev. B **98**, 224420 (2018).

[27] I. Mirebeau, N. Martin, M. Deutsch, L. J. Bannenberg, C. Pappas, G. Chaboussant, R. Cubitt, C. Decorse, and A. O. Leonov, Spin textures induced by quenched disorder in a reentrant spin glass: Vortices versus "frustrated" skyrmions, Phys. Rev. B **98**, 014420 (2018).

[28] A. A. Mistonov, I. S. Dubitskiy, I. S. Shishkin, N. A. Grigoryeva, A. Heinemann, N. A. Sapoletova, G. A. Valkovskiy, and S. V. Grigoriev, Magnetic structure of the inverse opal-like structures: Small angle neutron diffraction and micromagnetic simulations, J. Magn. Magn. Mater. **477**, 99 (2019).

[29] C. Kons, M.-H. Phan, H. Srikanth, D. A. Arena, Z. Nemati, J. A. Borchers, and K. L. Krycka, Investigating spin coupling across a three-dimensional interface in core/shell magnetic nanoparticles, Phys. Rev. Mater. **4**, 034408 (2020).

[30] D. Zákutná, D. Nižňanskỳ, L. C. Barnsley, E. Babcock, Z. Salhi, A. Feoktystov, D. Honecker, and S. Disch, Field dependence of magnetic disorder in nanoparticles, Phys. Rev. X **10**, 031019 (2020).

[31] L. G. Vivas, R. Yanes, D. Berkov, S. Erokhin, M. Bersweiler, D. Honecker, P. Bender, and A. Michels, Toward understanding complex spin textures in nanoparticles by magnetic neutron scattering, Phys. Rev. Lett. **125**, 117201 (2020).

[32] M. Bersweiler, M. P. Adams, I. Peral, J. Kohlbrecher, K. Suzuki, and A. Michels, Unraveling the magnetic softness in Fe–Ni–B-based nanocrystalline material by magnetic small-angle neutron scattering, IUCrJ **9**, 65 (2022).

[33] E. M. Jefremovas, M. de la Fuente Rodríguez, D. Alba Venero, C. Echevarría-Bonet, P. Bender, B. Fåk, J. A. Blanco, and L. Fernández Barquín, Magnetic super-structure and active surface role in the onset of magnetic excitons revealed in $TbCu_2$ nanoparticles, Commun. Mater. **4**, 56 (2023).

[34] C. Kons, K. L. Krycka, J. Robles, N. Ntallis, M. Pereiro, M.-H. Phan, H. Srikanth, J. A. Borchers, and D. A. Arena, Influence of hard/soft layer ordering on magnetization reversal of bimagnetic nanoparticles: Implications for biomedical/theranostic applications, ACS Appl. Nano Mater. **6**, 10986 (2023).

[35] V. Ukleev, F. Ajejas, A. Devishvili, A. Vorobiev, N.-J. Steinke, R. Cubitt, C. Luo, R.-M. Abrudan, F. Radu, V. Cros, N. Reyren, and J. S. White, Observation by SANS and PNR of pure Neel-type domain wall profiles and skyrmion suppression below room temperature in magnetic $[Pt/CoFeB/Ru]_{10}$ multilayers, STAM Methods **25**, 2315015 (2024).

[36] M. P. Adams, M. Bersweiler, E. M. Jefremovas, and A. Michels, MuMag2022: A software tool for analyzing magnetic field dependent unpolarized small-angle neutron scattering data of bulk ferromagnets, J. Appl. Cryst. **55**, 1055 (2022).

[37] Z. Li, R. Parsons, B. Zang, H. Kishimoto, T. Shoji, A. Kato, J. Karel, and K. Suzuki, Dramatic grain refinement and magnetic softening induced by Ni addition in FeB based nanocrystalline soft magnetic alloys, Scr. Mater. **181**, 82 (2020).

[38] C. D. Dewhurst, Graphical reduction and analysis small-angle neutron scattering program: *GRASP*, J. Appl. Crystallogr. **56**, 1595 (2023).

[39] D. Honecker and A. Michels, Theory of magnetic small-angle neutron scattering of two-phase ferromagnets, Phys. Rev. B **87**, 224426 (2013).

[40] D. Honecker, C. D. Dewhurst, K. Suzuki, S. Erokhin, and A. Michels, Analysis of magnetic neutron-scattering data of two-phase ferromagnets, Phys. Rev. B **88**, 094428 (2013).

[41] J. McCord and A. Hubert, Normalized differential Kerr microscopy an advanced method for magnetic imaging, Phys. Status Solidi A **171**, 555 (1999).

[42] A. Aharoni, *Introduction to the Theory of Ferromagnetism*, 2nd ed. (Oxford University Press, Oxford, 2000).

[43] A. Michels, Magnetic small-angle neutron scattering of bulk ferromagnets, J. Phys.: Condens. Matter **26**, 383201 (2014).

[44] F. Y. Ogrin, S. L. Lee, M. Wismayer, T. Thomson, C. D. Dewhurst, R. Cubitt, and S. M. Weekes, Micromagnetic simulation of small-angle neutron scattering from magnetic recording media, J. Appl. Phys. **99**, 08G912 (2006).

[45] A. Michels, C. Vecchini, O. Moze, K. Suzuki, J. M. Cadogan, P. Pranzas, and J. Weissmüller, Dipole-field–induced spin disorder in a nanocomposite soft magnet, Europhys. Lett. **72**, 249 (2005).

[46] A. Michels, C. Vecchini, O. Moze, K. Suzuki, P. K. Pranzas, J. Kohlbrecher, and J. Weissmueller, Temperature dependence of dipole-field scattering in Nanoperm, J. Magn. Magn. Mater. **316**, 448 (2007).

[47] A. Michels, F. Döbrich, M. Elmas, A. Ferdinand, J. Markmann, M. Sharp, H. Eckerlebe, J. Kohlbrecher, and R. Birringer, Spin structure of nanocrystalline gadolinium, Europhys. Lett. **81**, 66003 (2008).

[48] A. Michels, M. Elmas, F. Döbrich, M. Ames, J. Markmann, M. Sharp, H. Eckerlebe, J. Kohlbrecher, and R. Birringer, Porosity-induced spin disorder in nanocrystalline inert-gas-condensed iron, Europhys. Lett. **85**, 47003 (2009).

[49] A. Michels, R. N. Viswanath, J. G. Barker, R. Birringer, and J. Weissmüller, Range of magnetic correlations in nanocrystalline soft magnets, Phys. Rev. Lett. **91**, 267204 (2003).

[50] J.-P. Bick, D. Honecker, F. Döbrich, K. Suzuki, E. P. Gilbert, H. Frielinghaus, J. Kohlbrecher, J. Gavilano, E. M. Forgan, R. Schweins, P. Lindner, R. Birringer, and A. Michels, Magnetization reversal in Nd-Fe-B based nanocomposites as seen by magnetic small-angle neutron scattering, Appl. Phys. Lett. **102**, 022415 (2013).

[51] D. Mettus and A. Michels, Small-angle neutron scattering correlation functions of bulk magnetic materials, J. Appl. Crystallogr. **48**, 1437 (2015).

[52] S. Chikazumi, *Physics of Ferromagnetism* (Clarendon Press, Oxford, 1997), Chap. 16.

[53] J. M. D. Coey, *Magnetism and Magnetic Materials* (Cambridge University Press, Cambridge, 2009).

[54] M. F. Collins, V. J. Minkiewicz, R. Nathans, L. Passell, and G. Shirane, Critical and spin-wave scattering of neutrons from iron, Phys. Rev. **179**, 417 (1969).

[55] R. Skomski, Nanomagnetics, J. Phys.: Condens. Matter **15**, R841 (2003).

[56] D. Honecker, F. Döbrich, C. D. Dewhurst, A. Wiedenmann, and A. Michels, Neutron spin-flip scattering of nanocrystalline cobalt, J. Phys.: Condens. Matter **23**, 016003 (2011).